

**Please cite the Published Version**

Gubernat, A , Klimczyk, P , Pasierb, P, Rutkowski, P , Kornaus, K , Lach, R , Kulczyk-Malecka, J  and Morgiel, J (2025) High-pressure sintered polycrystals from Ti-coated cBN powders: microstructure, mechanical properties and thermo-electrical characteristics. *Journal of the European Ceramic Society*, 45 (11). 117393 ISSN 0955-2219

**DOI:** <https://doi.org/10.1016/j.jeurceramsoc.2025.117393>

**Publisher:** Elsevier BV

**Version:** Accepted Version

**Downloaded from:** <https://e-space.mmu.ac.uk/639468/>

**Usage rights:**  [Creative Commons: Attribution 4.0](https://creativecommons.org/licenses/by/4.0/)

**Additional Information:** This is an author accepted manuscript of an article published in *Journal of the European Ceramic Society*, by Elsevier. This version is deposited with a Creative Commons Attribution 4.0 licence [<https://creativecommons.org/licenses/by/4.0/>], in accordance with Man Met's Research Publications Policy. The version of record can be found on the publisher's website.

**Enquiries:**

If you have questions about this document, contact [openresearch@mmu.ac.uk](mailto:openresearch@mmu.ac.uk). Please include the URL of the record in e-space. If you believe that your, or a third party's rights have been compromised through this document please see our Take Down policy (available from <https://www.mmu.ac.uk/library/using-the-library/policies-and-guidelines>)

# High-pressure sintered polycrystals from Ti-coated cBN powders: microstructure, mechanical properties and thermo-electrical characteristics

Agnieszka Gubernat<sup>1</sup>, Piotr Klimczyk<sup>2\*</sup>, Paweł Pasierb<sup>1</sup>, Paweł Rutkowski<sup>1</sup>, Kamil Kornaus<sup>1</sup>, Radosław Lach<sup>1</sup>, Justyna Kulczyk-Malecka<sup>3</sup>, Jerzy Morgiel<sup>4</sup>

<sup>1</sup> AGH University of Krakow, Faculty of Materials Science and Ceramics, Krakow, Poland

<sup>2</sup> Łukasiewicz Research Network, Krakow Institute of Technology, Krakow, Poland

<sup>3</sup> Manchester Metropolitan University, Manchester Fuel Cell Innovation Centre, Surface Engineering Group, UK

<sup>4</sup> Institute of Metallurgy and Materials Science, Polish Academy of Sciences, Krakow, Poland

\*Corresponding author, e-mail: [piotr.klimczyk@kit.lukasiewicz.gov.pl](mailto:piotr.klimczyk@kit.lukasiewicz.gov.pl)

## Abstract

Three grades of Ti-coated cubic boron nitride (cBN) powders, differing in grain size and coating thickness, were used to produce high-pressure, high-temperature (HPHT) sintered polycrystalline materials (PcBN) without the addition of any bonding phase. The sintered materials were thoroughly characterized, including assessments of basic physical and mechanical properties, microstructure and phase composition. Furthermore, the electrical and thermal properties of the sintered bodies were investigated.

The resulting materials are nearly pore-free polycrystalline composites, characterized by a Young's modulus ranging from 620 to 850 GPa and exceptionally high hardness values between 30 and 67 GPa, depending on the powder used. Phase and microstructural analysis revealed that the composites consisted of cBN grains uniformly surrounded by titanium compounds such as TiN and TiB<sub>2</sub>. These compounds were formed just during the powder coating stage due to the high reactivity of titanium with cBN. Further crystallization of titanium phases occurred during the HPHT process. Impedance spectroscopy and laser flash analysis demonstrated that microstructure and phase composition significantly affect the electrical and thermal conductivities of these materials. Additionally, substantial changes in these properties with temperature were observed.

Due to their favourable properties, these composites can be considered promising candidates for use in advanced cutting tools. This is especially relevant in ongoing research on smart tools capable of self-diagnosing wear status based on changes in electrical properties during cutting.

## Keywords

polycrystalline cubic boron nitride, titanium compounds, high pressure – high temperature, mechanical properties, microstructure, laser flash analysis, electrochemical impedance spectroscopy

## 1. Introduction

Cubic boron nitride (cBN) is classified as a superhard material known for its exceptional wear resistance. The two primary areas of applications of this material are linked with production of grinding and cutting tools [1,2]. In the first case the cBN crystals are bonded using resins, metals, or just vitrified phases, while in the second one the activation of the sintering process allowing to obtain polycrystalline cBN (PcBN) is in need.

The superabrasive cBN grit has shown an excellent performance in high-speed grinding of strong and tough materials, such as Ni-based superalloys and Ti alloys. Additionally, the cBN grinding wheels are often used for wet or dry processing of hard machine parts made of metal matrix composites, like wire drawing carbide dies. Such treatments are applied whenever the precision finish is required including automotive, aviation and medical industries [3–7].

The sintered PcBN, along with various composite materials derived from it, are widely employed to produce cutting inserts for machining difficult-to-cut materials [8–10]. However, the cBN is a metastable phase and therefore its sintering could be successfully achieved at the High Pressure – High Temperature (HPHT) conditions (5–8 GPa, ~2200 °C) [11]. The admixing of Al or Ti powders into cBN powders helps to reduce the sintering temperature of composite material by activation of reactive sintering mechanisms [12]. The ceramic phases such as AlN, TiN or TiB<sub>2</sub>, formed during these processes, allow to improve some of the properties of cBN composites, like their thermal stability and resistance to chemical wear [13–16].

Cubic BN powders are commercially available as base or coated with Ni, Cr, Ti or Cu ones. Metal coatings were developed mainly for grinding tools production technology to enhance cBN retention in the bonding matrix and increase their thermal stability that provides improved surface integrity in the grinding of hardened alloy steels, tool steels, and nickel- and cobalt-based superalloys [17–19].

The Ti - due to its high reactivity with BN [20,21] – tend to form over such crystallites a compound layer, what prompted to call it an active coating technology (ACT) [6]. Even, as most of coated powders are presently aimed for fabrication of grinding tools, though the ACT may also help produce the material for cutting inserts of improved mechanical properties. The use of coated cBN powders eliminates the need for a mixture preparation step and prevents the formation of agglomerates in the bonding phase during the manufacturing of composites (agglomeration is often unavoidable when relying on mechanical mixing of the respective powders prior to the sintering process). Direct compacting of uniformly coated powders not only cuts on fabrication time but also enhance material strength by eliminating agglomerates.

In this work, Ti-coated cBN powders were used to obtain PcBN bulk materials sintered without any additional bonding phase. The sintered composites were thoroughly characterized across several key dimensions. This included an assessment of basic physical and mechanical properties such as apparent density, Young's modulus and hardness. Additionally, the microstructure and phase composition were analysed using advanced techniques, including Scanning Electron Microscopy (SEM), Scanning Transmission Electron Microscopy with Energy Dispersive Spectroscopy (STEM/EDS), and X-ray Diffraction (XRD).

Furthermore, the electrical properties were evaluated through Electrochemical Impedance Spectroscopy (EIS), while thermal properties were determined using Laser Flash Analysis (LFA).

## 2. Materials and methods

### 2.1. Characteristics of starting powders

Two commercial powders of Ti-coated cBN: CBN-B-TA grade, 6-12  $\mu\text{m}$ , Van Moppes, Switzerland and CeraMicron CM-CBN 80 Ti grade, 20-30  $\mu\text{m}$ , Ceratonia, Germany were used in these experiments (coded as cBN-VM and cBN-CM, respectively). Their detail microstructure characterization helped to establish that practically all powder particles were covered by coatings of thickness of  $\sim 200$  nm (cBN-VM) and  $\sim 800$  nm (cBN-CM), as described elsewhere [22] (Fig. 1). Additionally, an in-house Ti-coated cBN powder coded as cBN-0 (ABN M36 grade, 3-6  $\mu\text{m}$ , by Element Six, Ireland) was produced using magnetron sputtering technique. The deposition process was started by pumping the system down to  $9.6 \times 10^{-4}$  Pa base pressure and next backfilled with Ar at a flow rate of 30 sccm (setting dynamic pressure at 0.25 Pa). The titanium cathode was sputtered in pulsed DC mode at 800 W applied power, 100 kHz pulse frequency at 60% duty using Advanced Energy Pinnacle Plus power supply. The cBN powders were placed in an oscillating substrate holder under the magnetrons allowing powders to roll, as described in Shaw et al. [23].

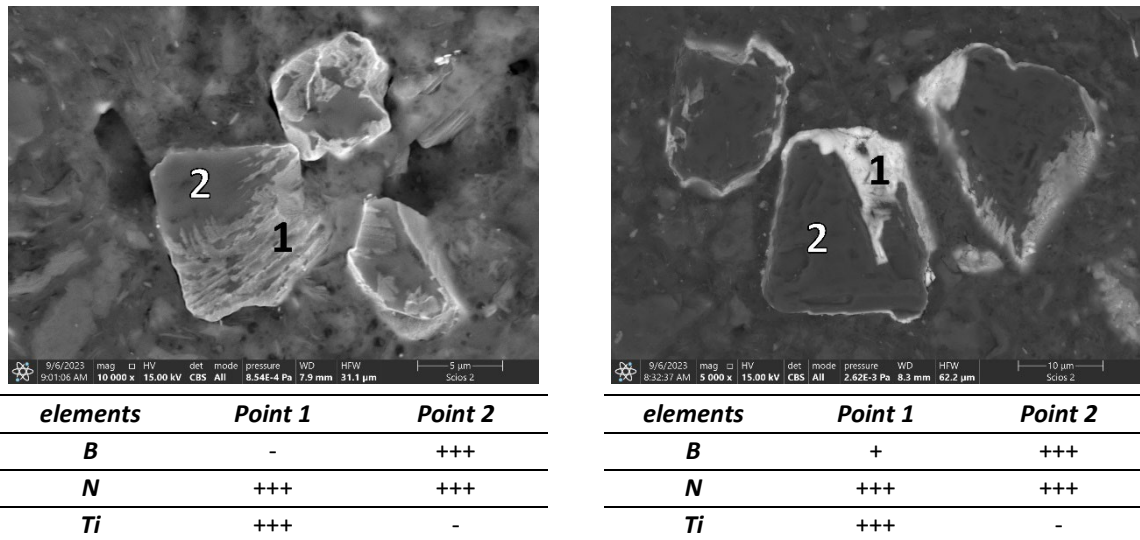


**Fig. 1.** Morphologies (SEM) of Ti-coated cBN powders: cBN-VM (a) and cBN-CM (b) (+++ substantial amount; ++ mean amount; + trace amount).

The phase content of respective phases measured in the investigated powders with XRD/Rietveld method was given in Table 1.

**Table 1.** Quantitative phase composition of Ti-coated cBN powders.

Powder	Quantitative analysis, mass %
cBN-0	98.2 % cBN, 0.7% Ti, 1.1% TiN

cBN-VM	91.0 % cBN, 2.8% Ti, 6.2% TiN
cBN-CM	85.4% BN, 0.5% Ti, 7.6% Ti <sub>2</sub> N, 6.5% TiB

## **2.2. High pressure and high temperature sintering procedure HPHT**

HPHT sintering process was carried out with the help of the Bridgman-type toroidal apparatus. In this system a quasi-isostatic compression of the preliminary consolidated powders is achieved as a result of plastic deformation of the mineral gasket material (usually metamorphic stones) inserted between anvils [24,25]. Electrical heating of the sample material is provided by a high-power current transformer and graphite heater.

The Ti-coated cBN powders were pressed into cylindrical pellets ( $\phi$  - 12 mm, height; 5 mm) under the pressure of 200 MPa. Next, the pellet was placed into the graphite heater in the central part of the HPHT cell assembly. The final consolidation was carried out at the pressure of 7.7 GPa and the temperature of 2200 °C. The HPHT sintering process lasted 60 s.

## **2.3. Measurement and characterisation of sinters**

The apparent density of the sintered samples was measured with the Archimedes method in distilled water using an analytical balance equipped with a standard density determination kit. The Young's modulus was determined via the ultrasonic wave transition method by using the Panametrics Epoch III ultrasonic flaw detector. Elastic constants were calculated basing on the densities of materials and the velocities of longitudinal and transverse waves passing through the samples. The hardness was measured by the Vickers indentation method by applying loads of 9.81 N (1 kg) using a Future Tech FLC-50VX hardness tester. For each sample, five indentations were made.

The average phase composition was assessed using X-ray diffraction (XRD) method. The spectra were acquired using a X'Pert PANalytical Empyrean diffractometer with Cu radiation ( $\lambda_{Cu} = 1.5406\text{\AA}$ ). The fraction of respective phases was determined using Rietveld refinement and HighScore PANalytical software. The overview of the microstructure of sinters was documented from polished sections of the pellets using a scanning electron microscope (SEM) Scios 2 (ThermoFisher). The microstructure details concerning location of various phases within the bonding phase and at surface of the cBN particles were characterized with probe corrected Themis (200kV) FEG transmission electron microscope (TEM) equipped with 4-segmented X-ray EDS detector (ThermoFisher). The distribution of involved elements was presented using net counts (background removed) on maps built of 500 x 500 pixels. The thin lamellae for these observations were prepared with focused ion beam (FIB) method.

The electrical conductivity of samples was measured using the Electrochemical Impedance Spectroscopy (EIS) technique with a Solartron 1260 Frequency Response Analyzer (FRA) coupled with the Solartron 1296 Dielectric Interface. It was carried out with Pt electrodes and in the frequency range 10 – 10<sup>6</sup> Hz, at 10 points per decade, with a sinusoidal voltage amplitude of 20 mV. The impedance was tested in the temperature range from 20 °C to 850 °C, in the flow of Ar gas as a protective atmosphere (flow rate 60 sccm, set by MKS flow controllers). Each sample was tested at least twice for ascending and descending

temperatures, in order to evaluate the reproducibility of the results. Interpretation of the obtained data was performed using ZView software (Scribner Asc., USA).

The thermal diffusivity of sinters was checked with LFA 427 of Netzsch (Selb, Germany) set using 10 mm diameter alumina centring cone and sample thickness  $\sim 5$  mm. The measurement was made in 150 ml/min argon flow, 0.5 ms pulse width and 600 V laser voltage. The laser shots were made at 20, 100, 300, 500, 700 and 900°C. In order to analyse collected data and calculate specific heat capacity the Proteus v. 4.8.5 version Netzsch Analysis software was applied. For thermal diffusivity determination the Cape-Lehman + ps model used. The pure copper (99.95) was used as a reference sample. The specific heat capacity was calculated by using comparison method, i.e. comparing tested sample and reference material in exactly the same conditions. The uncertainty of thermal diffusivity calculation was 0.8% for room temperature (RT) and 0.4% for highest temperature measurement. Correlation coefficient of model fitting was 0.997 and 0.999 for high temperature, where signal is usually smoother.

### 3. Results

#### 3.1. Physical and mechanical properties

The un-aided eye check of the produced sinters proved them free of any macroscopic defects like cracks or any surface voids. The measurements of the densities, Young's moduli and hardness of the PcBN compacts were given in (Table 2).

**Table 2.** Basic physical and mechanical properties of sintered compacts.

Sintered body	Apparent density g/cm <sup>3</sup>	Young's modulus GPa	Vickers hardness (HV1), GPa
cBN-0	3.49 ± 0.02	850 ± 15	47.7 ± 5.8
cBN-VM	3.60 ± 0.02	780 ± 19	29.3 ± 1.8
cBN-CM	3.67 ± 0.02	621 ± 10	66.8 ± 26.1

The cBN-0 sample density and Young's modulus that were closest to the theoretical values for pure cBN, which are 3.48 g/cm<sup>3</sup> and 909 GPa [26,27], respectively. It confirms that the cBN-0 sample contained the smallest amount of Ti and/or Ti compounds. The cBN-VM and cBN-CM samples have higher densities and lower Young's moduli, respectively, which is consistent with the higher content of Ti and/or Ti compounds. Titanium, as well as its borides and nitrides have a density in the range of 4.5-5.4 g/cm<sup>3</sup> [28,29], being again noticeably higher than that of the cBN phase. Simultaneously, these Ti compounds have a Young's modulus in the range of 430-550 GPa [28,29], what is well below that characteristic for the cBN. A different behaviour was noted in case of hardness of the tested samples, as the highest one showed the cBN-CM sample accompanied by large results scatter. This was due to the large size of the cBN crystallites in these sinters, as compared with the tip of the Vickers indenter. In such situation, test involving the cBN grain gave high HV read-outs, comparable to the theoretical hardness of cBN ( $\sim 70$  GPa [30,31]). On the contrary, when the indenter hits the cBN crystallite side or bonding phase, a much lower values of HV, close to that of the TiN/TiB<sub>2</sub> phases (20-30

GPa [32]) were obtained. In the case of cBN-0 and cBN-VM samples, the cBN crystallite size was smaller and therefore the measurements represented the averaged hardness of the composite [31,33].

### 3.2. XRD phase analysis

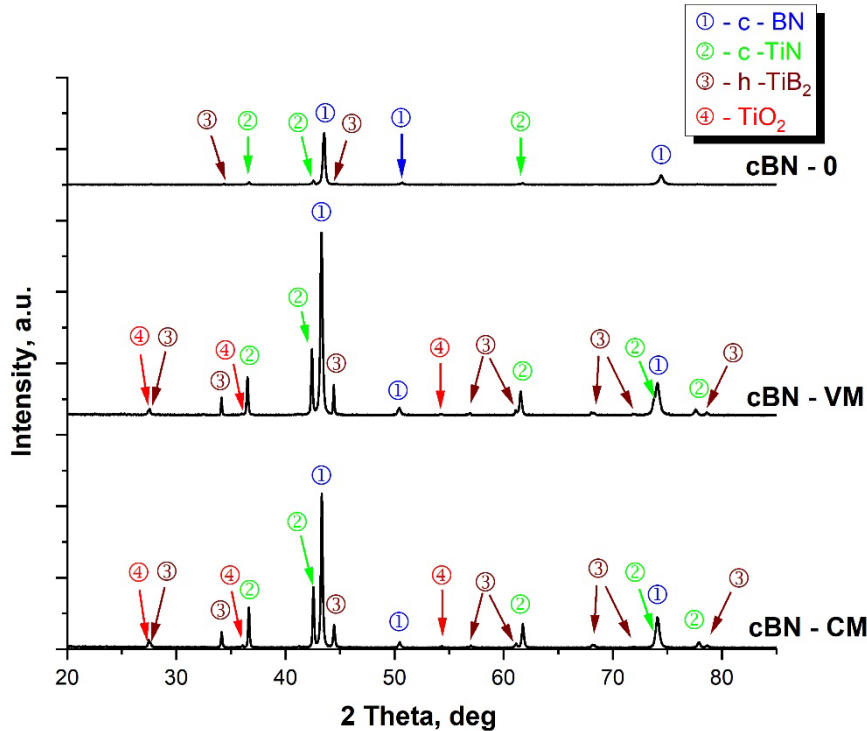


**Fig. 2.** X-ray diffraction patterns of cBN-VM, cBN-CM and cBN-0 HPHT sintered body.

The XRD spectra acquired from as-sintered materials showed, that after HPHT processing aside of cBN phase they also contain a share of nitrides and borides (Fig. 2). Namely, a spectrum from the cBN-VM sample showed not only strong peaks originating from regular boron nitride, but also weak ones from TiN, TiB<sub>2</sub> and rutile-structured TiO<sub>2</sub>. An additional quantitative assessment of that spectra helped to establish that the TiB<sub>2</sub> occupies 2%, the TiN 6%, while TiO<sub>2</sub> was present in trace amounts of up to 0.5%. The similar situation took place in case of cBN-CM sintered material in which TiN, TiB<sub>2</sub> and rutile-structured TiO<sub>2</sub> phases were represented at the level of 4%, 8% and 0.4%, respectively. Generally, for both composites these values are close to that measured for the pre-sintered coated cBN-VM powder [22]. It is noteworthy that within a very short sintering time (~1 minute) the titanium boride TiB<sub>2</sub> and TiO<sub>2</sub> with a rutile structure were grown. The presence of the newly formed phases indicates the activation of a reaction between the cBN and the titanium-rich layer.

XRD measurements of the phase composition of titanium-coated cBN-0 powder under laboratory conditions also showed the presence of TiB<sub>2</sub> and TiN (Fig. 2). No rutile or any other titanium oxide phase was detected, indicating that the coating does not oxidise during the sintering process. The total amount of both compounds is approx. 2 wt% (see table 3).

**Table 3.** Quantitative phase composition of cBN sinters.

Sintered body	Quantitative phase analysis, mass %
cBN-0	97.9% cBN, 0.3% TiB <sub>2</sub> , 1.8% TiN,
cBN-VM	90.7% cBN, 2.4% TiB <sub>2</sub> , 6.4% TiN, 0.5% TiO <sub>2</sub> (rutile)
cBN-CM	87.3% cBN, 3.9% TiB <sub>2</sub> , 8.1% TiN, 0.7% TiO <sub>2</sub> (rutile)

### 3.3. SEM and SEM/EDS studies

SEM observations of polished sections of the cBN-0, cBN-VM and cBN-CM sinters confirmed, that the first one was built of significantly smaller crystallites than the last two (to compare Fig. 3 at Fig. 4a). At the same time the cBN-VM material was characterized by most uniform distribution of binder material covering practically all cBN grain boundaries, while in the cBN-CM one a presence of aggregates of binder phase were noted.

In the case of cBN-0 polycrystal, no titanium bonding material was observed at some of the grain boundaries (Fig. 4). The corresponding EDS mapping showing the distribution of the involved elements only confirmed the dominant contribution of Ti in the bonding phase (Figs. 5-7). The mapping obtained from the cBN-CM sinter (Fig. 7) indicated the presence of a chemical composition gradient within the binding phase. In the case of cBN-0, these measurements also confirmed the absence of Ti or Ti compounds at some cBN grain boundaries (Fig. 5).

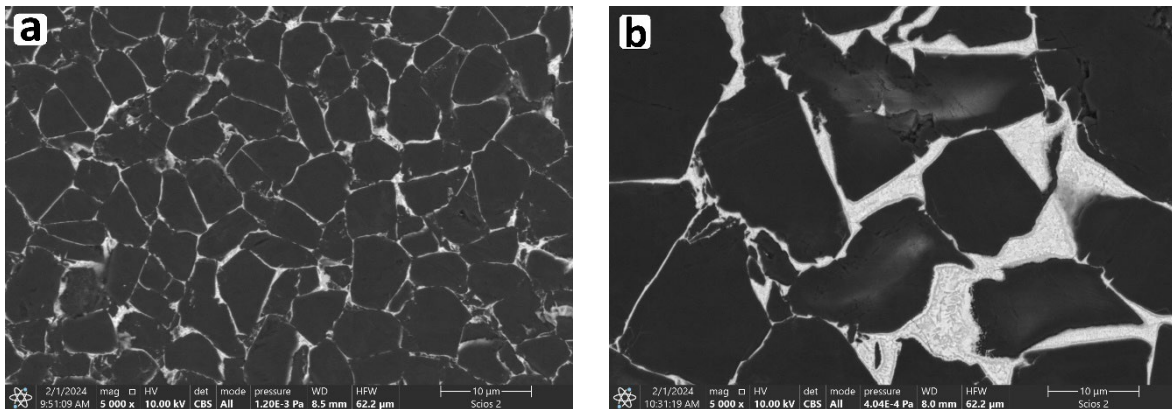


**Fig. 3.** SEM images presenting overview of microstructure of cBN-VM (a) and cBN-CM (b) sinters.

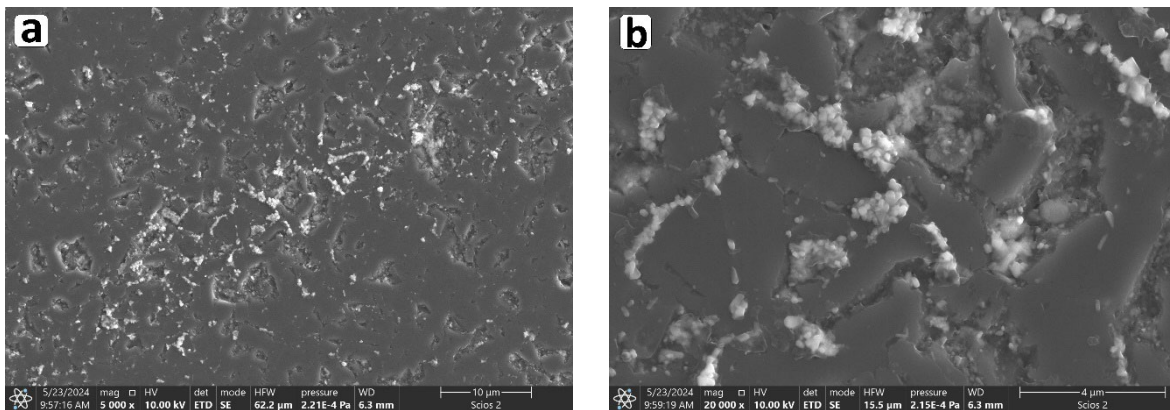


**Fig. 4.** SEM images overview of cBN-0 sinter: (a) low and (b) high magnification, respectively

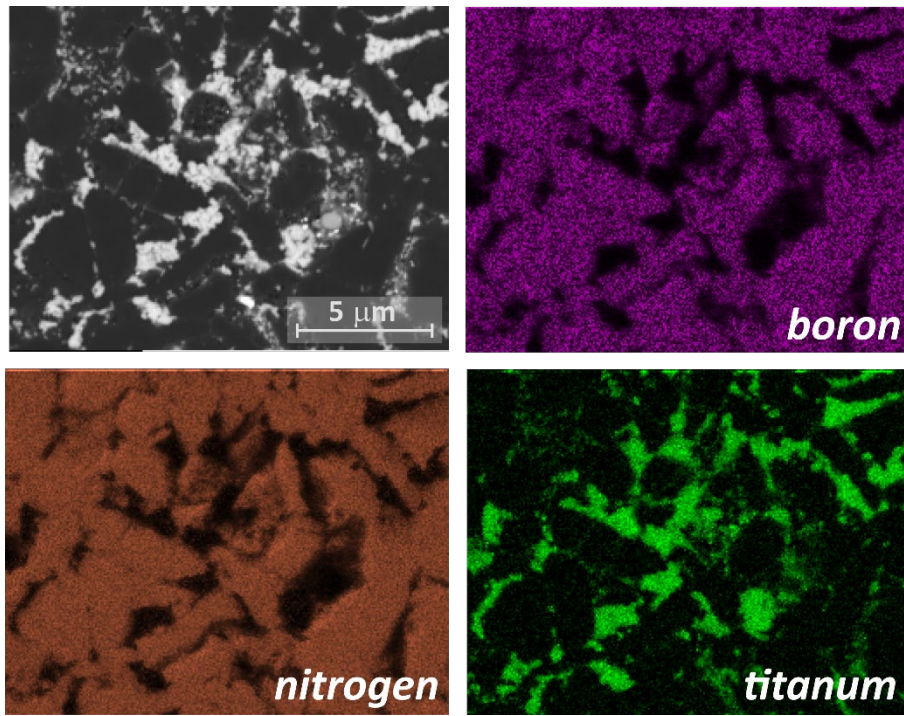


*Fig. 5. SEM image and B, N and Ti distribution maps in cBN-0 polycrystal.*

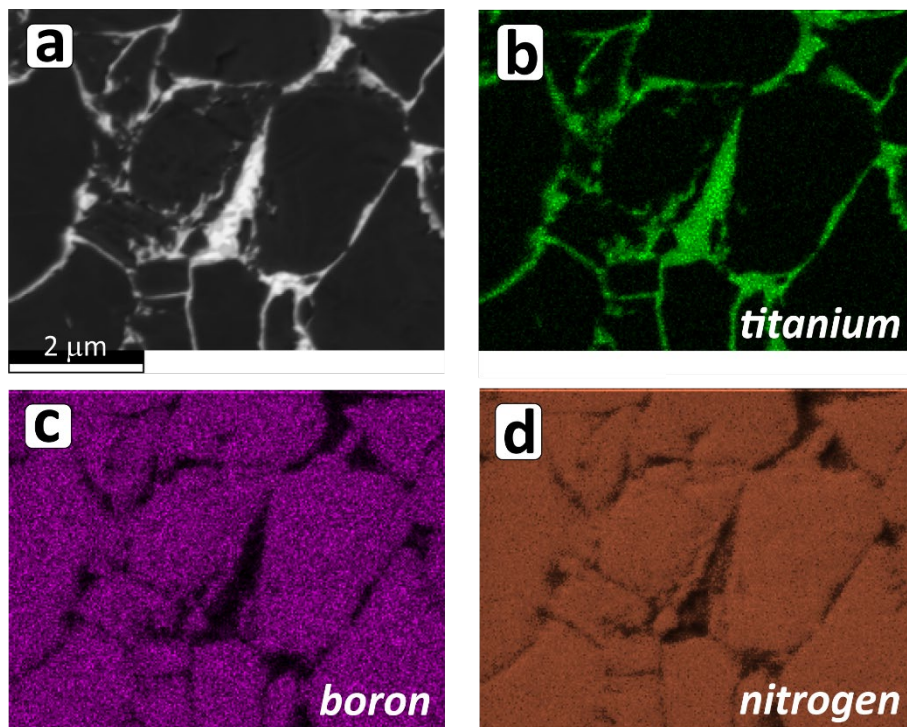


*Fig. 6. SEM image (a) and Ti (b), N (c) and B (d) maps of cBN-VM sintered body.*

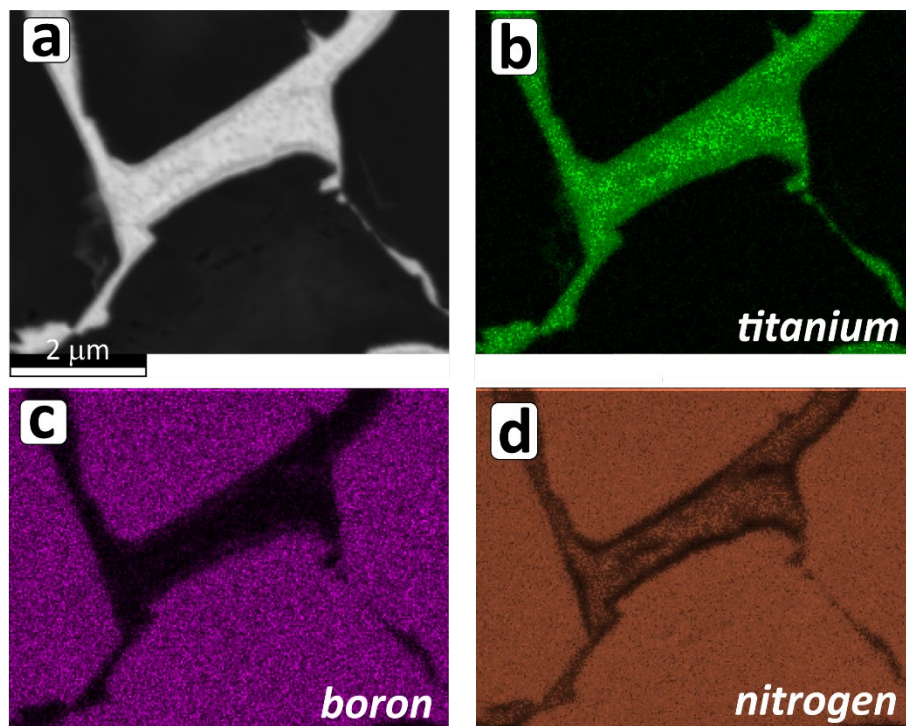
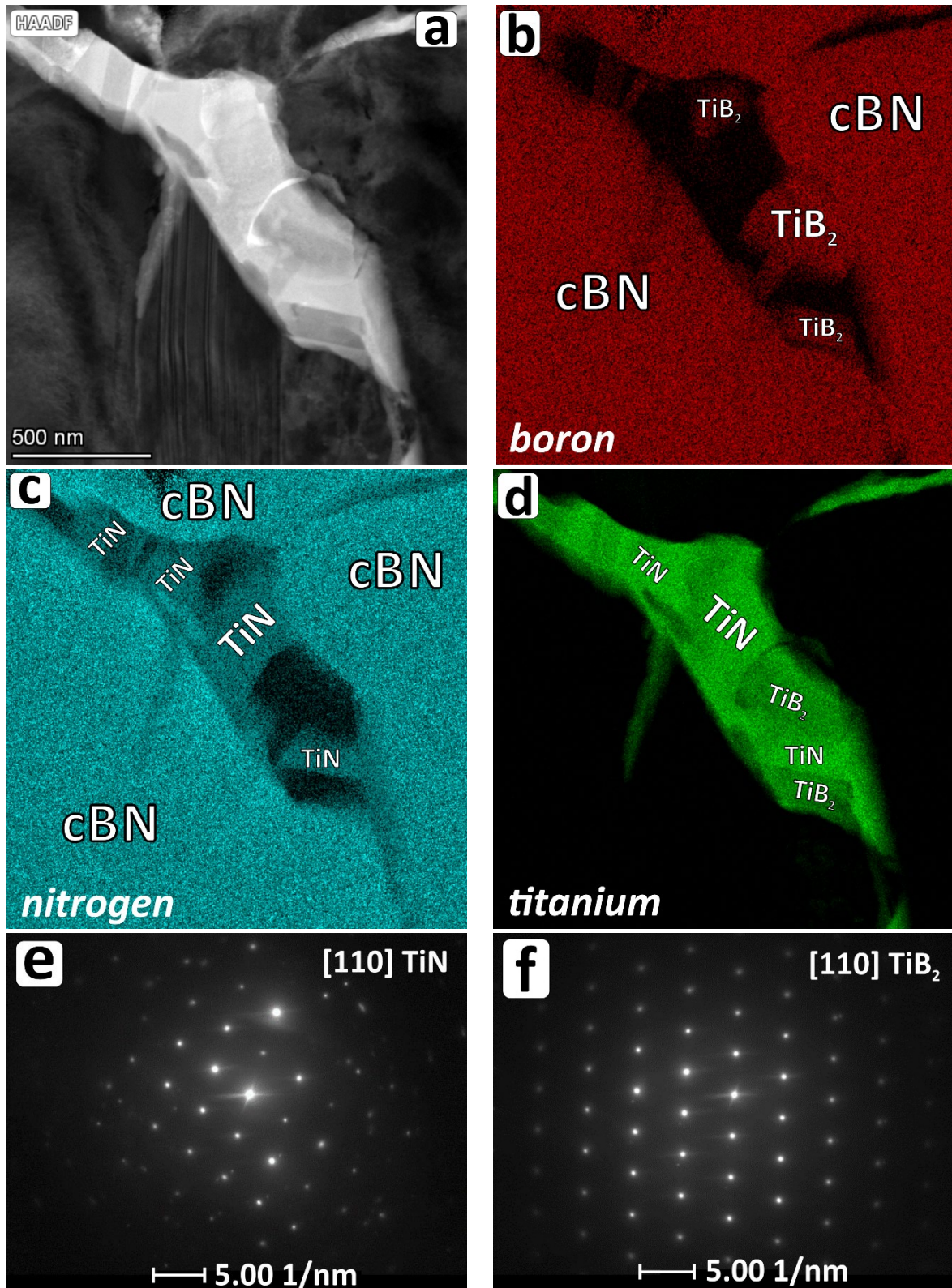


**Fig. 7.** SEM image (a) and Ti (b), N (c) and B (d) maps of cBN-CM sintered body.

### 3.4. STEM/EDS and TEM/ED studies

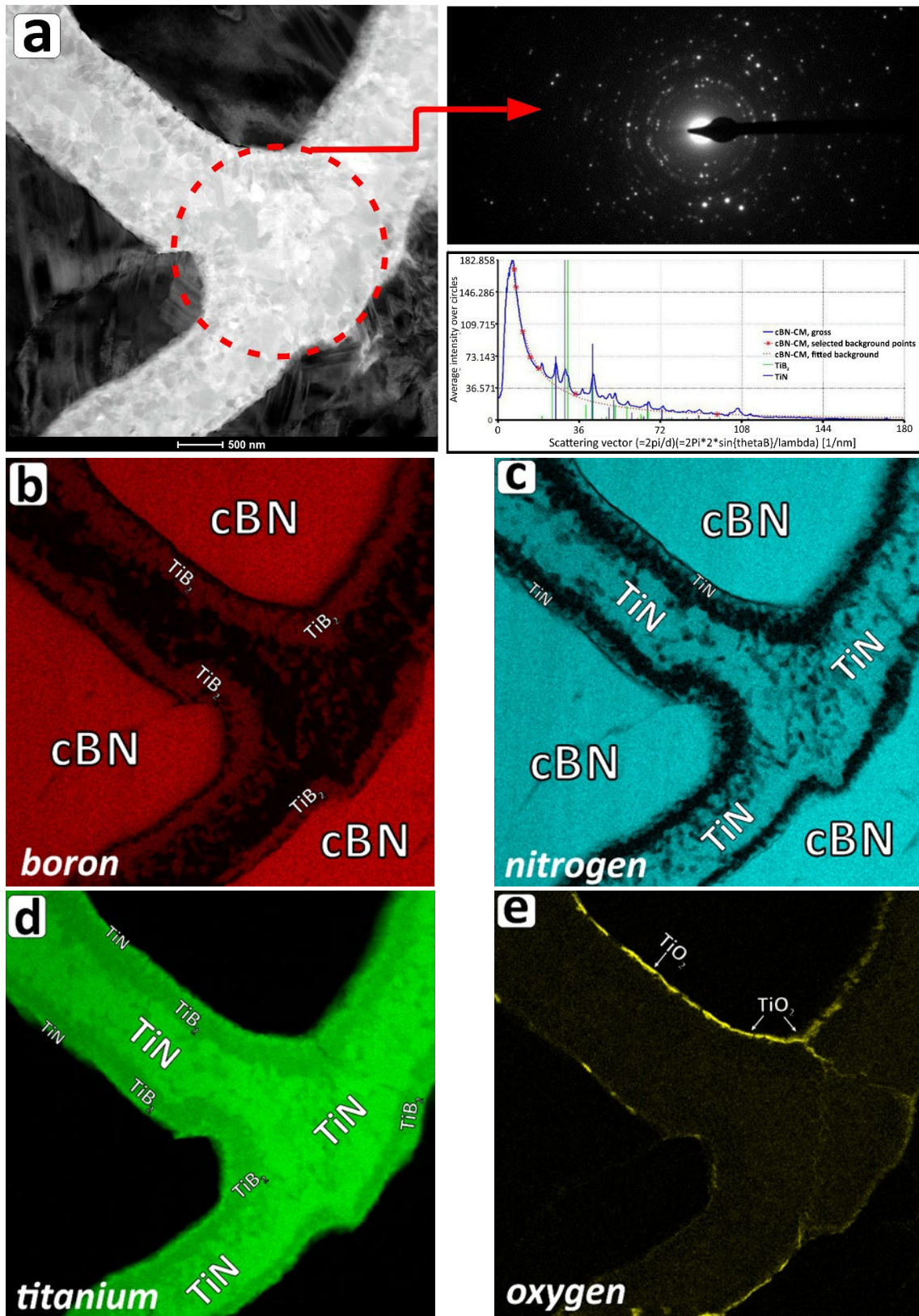
STEM observations of the sinters (cBN-VM) microstructure showed that the binder phase consisting of relatively coarse ( $0.1\ \mu\text{m} - 0.4\ \mu\text{m}$ ) grains was well coherent with the adjoining cBN crystallites, i.e. the boundary between both phases was free from defects or porosity (Fig. 8). The accompanying maps presenting distribution of B, N and Ti obtained using STEM/EDS technique proved that the binder is formed of a mixture of nitride and boride phases. The selected area electron diffraction patterns obtained from the N-rich and B-rich crystallites allowed to identify them as TiN and  $\text{TiB}_2$  phases, respectively (Figs 8e and 8f).

The same type of investigation of the cBN-CM sinter showed that in this case the binder was built of finer crystallites (at some places of columnar form) lining its boundary with the cBN (Fig. 9). The center of binder areas was occupied by larger roughly equiaxed grains approaching  $0.5\ \mu\text{m}$ . The STEM/EDS measurements indicated that boundary in-between the binder and the cBN is frequently occupied by layers of  $\text{TiO}_x$  (separately confirmed by concentration profile measured across one of binder channels presented in Fig. 9e). Within the binder, first a layer of very fine titanium nitride grains was found, which was followed by a layer coarser titanium boride. The center of binder channels was occupied again by the titanium nitride phase, but made of much coarser grains. Occasionally, in such areas the titanium borides were also found, but of much smaller size. The selected area electron diffraction acquired from the binder area filled with all these crystallites proved, that independently from their size or location, i.e. closer or more distant from the boundary with the BN crystallites, they still belong either to TiN or  $\text{TiB}_2$  type phase (Figs 9f and 9g).

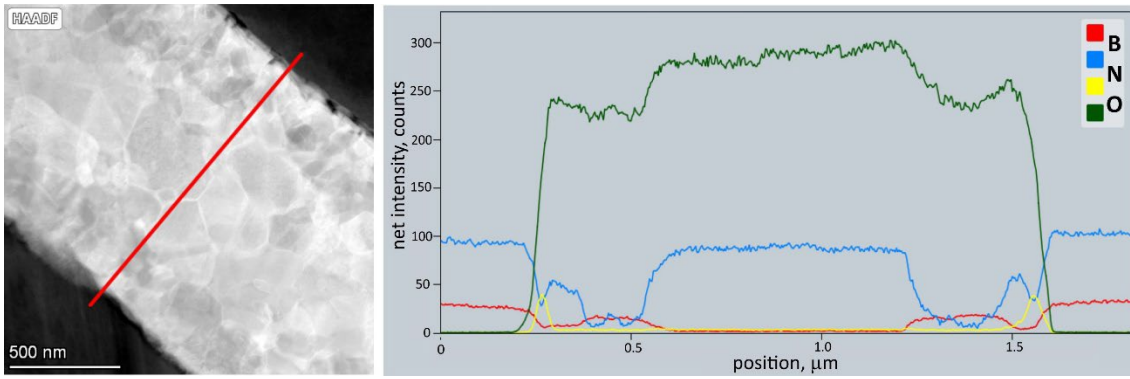


**Fig. 8.** STEM image of cBN-VM sinter microstructure (a), STEM/EDS maps presenting distribution of B (b), N (c), Ti (d) and electron diffractions from nitride (e) and boride crystallites (f).

The performed investigation indicates that in case of cBN-VM the crystallites from the binder spread over powder particles underwent just coarsening process. Though, the binder microstructure presented by the cBN-CM sinter, could have been developed only through its reaction with the cBN crystallites itself.

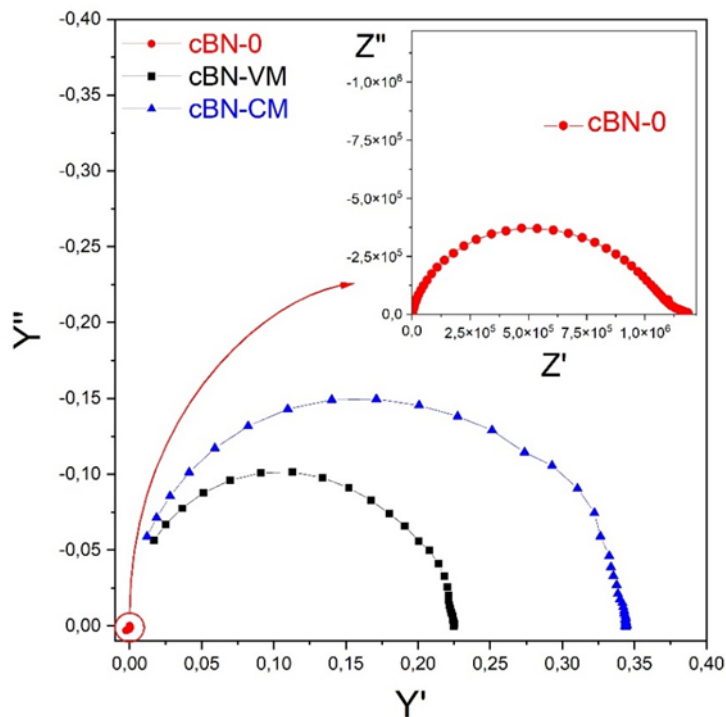


**Fig. 9.** STEM image of cBN-CM sinter microstructure with accompanying diffraction pattern and its solution (a) and STEM/EDS accompanying maps presenting distribution of B (b), N (c), Ti (d) and O (e).



**Fig. 10.** STEM/EDS line profile of composition of binder located in one of channels in cBN-CM sinter.

### 3.5. Impedance spectroscopy EIS



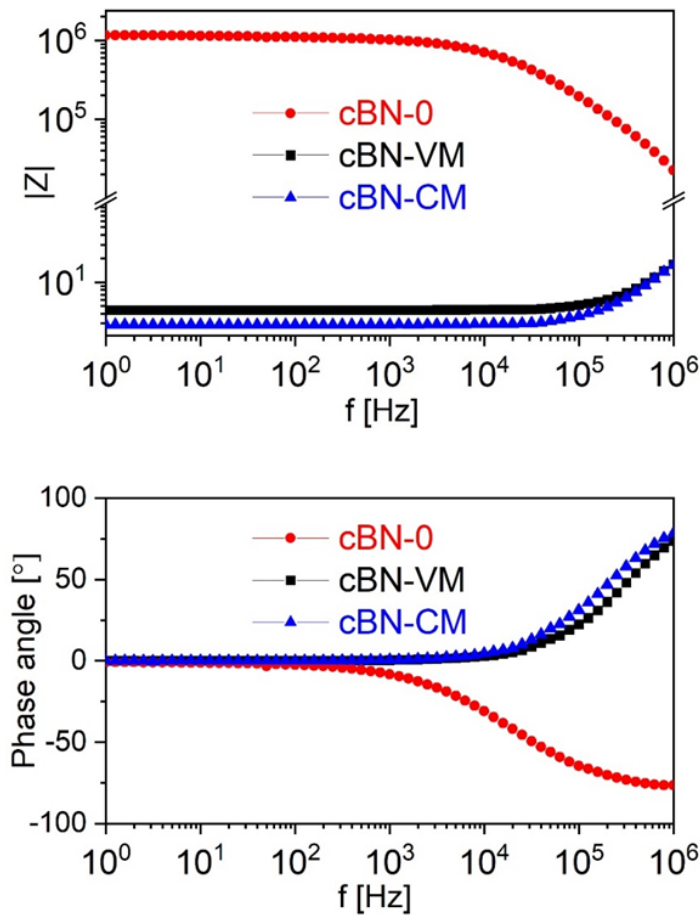
**Fig. 11.** Representative Nyquist plot measured at  $T = 700\text{ }^{\circ}\text{C}$ , shown in admittance (cBN-VM and cBN-CM) and impedance (cBN-0, inset) coordinates.

Figure 11 and Figure 12 shows representative Nyquist and Bode plots of EIS spectra obtained for cBN-VM, cBN-0 and for cBN-CM samples, measured at  $T = 700\text{ }^{\circ}\text{C}$ . The obtained EIS spectra consist of one semicircle only, which was observed in whole temperature range (200–850  $^{\circ}\text{C}$ ). These data were fitted with the ZView v3.5 (Scribner Asc., USA) software using an equivalent circuit composed from the resistance (R) connected in parallel with capacitance (C). The determined R values and the geometry of the samples were used to calculate the specific conductivities, according to the formula:

$$\sigma = \frac{d}{R \cdot s} \quad (1)$$

where:  $\sigma$  - specific conductivity,  $d$  - sample thickness,  $R$  - electrical resistivity,  $s$  - electrode surface area.

The specific conductivities for all the samples, in  $\log \sigma = f(1/T)$  coordinates was shown in Fig. 13.



**Fig. 12.** Bode plots of impedance module  $|Z|$  and phase angle determined for cBN-VM, cBN-CM, and cBN-0 samples at  $T = 700$  °C

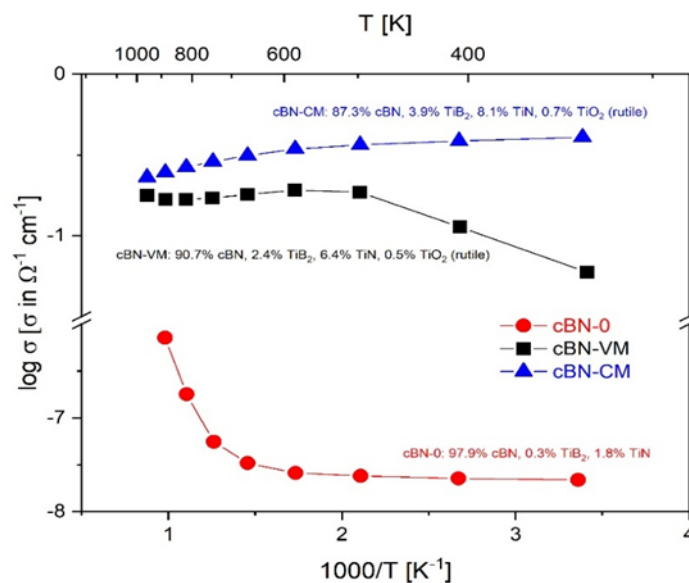


**Fig. 13.** Logarithm of specific conductivity as a function of reciprocal temperature determined for cBN-0, cBN-VM and cBN-CM samples. Phase composition of materials is shown for reference

### 3.6. Thermal conductivity

The thermal diffusivity of measured materials is presented in Fig. 14. Thermal diffusivity was highest for reference cBN-0 material with lowest amount of titanium nitride and titanium additives. Towards to pure cBN thermal diffusivity is lower for cBN-0 sample because of material defects (grain boundaries, other phases etc.) The addition of titanium base phases to the material decreases thermal diffusivity. The difference in thermal diffusivity between reference cBN-0 and cBN-VM/CM differs by  $10.8 \text{ mm}^2/\text{s}$  ( $\sim 20 \%$ ). Comparing cBN-VM and cBN-CM, the heat transport represented by this parameter varies only by  $3.2 \text{ mm}^2/\text{s}$ , which may depend on grain size, various defects, phase composition and their volume fraction. Because cBN-VM has 3.4 mass % more cBN phase than cBN-CM and its thermal diffusivity is lower, therefore it should be the differences in grain size distribution of both major phase and additives, relative density and in fraction of titanium base phases. The highest thermal diffusivity values were obtained for cBN-CM material (characterized by largest grain size) for temperatures below  $100 \text{ }^\circ\text{C}$  ( $373 \text{ K}$ ), so low content of planar defect present in the cBN should have been decisive in this case (Fig. 15). Above this temperature the decrease in thermal diffusivity is also similar for both of the samples CM and VM. The presented in Fig. 15 data of specific heat capacity ( $c_p$ ) were experimentally measured for cBN-VM and cBN-CM samples. In case of reference cBN-0 material the  $c_p$  values versus temperature were taken from literature data [34][35] due to high difference in material dimension of sample to reference (Copper) in LFA measurement method. The cBN-0, cBN-VM and cBN-CM materials has also similar specific heat capacity values at room temperature. The values of  $c_p$  are lower at higher temperatures for samples with higher addition of titanium base phases in comparison with reference material. In accordance with equation (2) the density and specific heat capacity has influence on thermal conductivity values.

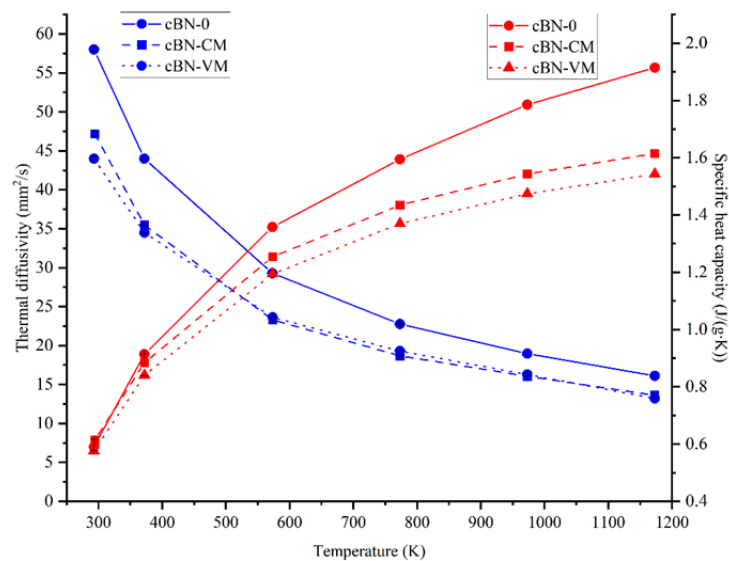


**Fig. 14.** Thermal diffusivity and calculated specific heat capacity of cBN-0, cBN-VM and cBN-CM samples.

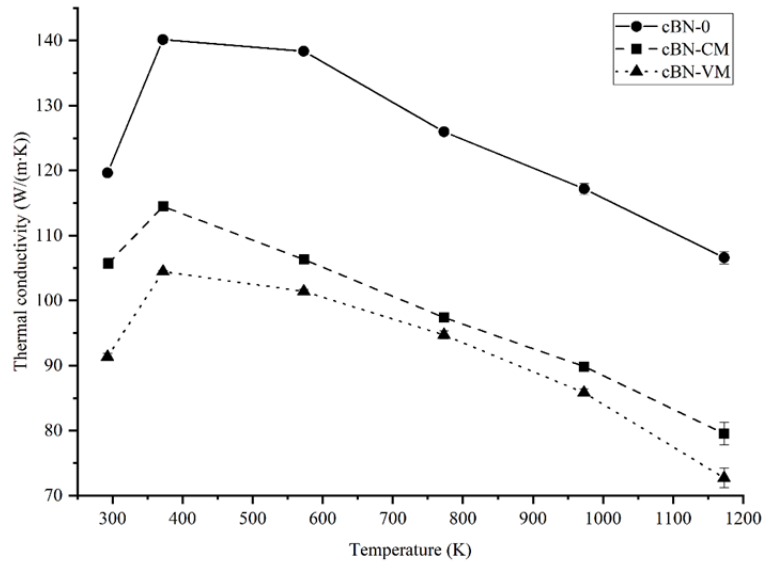


**Fig. 15.** Thermal conductivity of cBN-0, cBN-VM and cBN-CM samples.

The cubic boron nitride grains were a main phase of composite and their content and grain size distribution has an impact on thermal properties values in case of cBN-VM and cBN-CM materials. The reference cBN-0 sample showed also lower thermal properties values as compared to pure dense polycrystalline cBN [36][35], because of inhomogeneity in microstructure with differently distributed Ti based phases (Fig. 4). The cBN-VM sample characterized with average 9  $\mu\text{m}$  grain size and coarser CM with average 25  $\mu\text{m}$  particles also showed differences, in thermal properties (Fig. 14 and 15). In case of cBN-VM materials lower thermal properties were due to higher boundaries content and following it phonon wave scattering. In both of cases of material the thermal diffusivity decreases exponentially (Fig. 14), what means that flat and point defects play significant role in phonon scattering. In case of thermal conductivity an increase at 100  $^{\circ}\text{C}$ , curve shape, is similar to presented in case of metal matrix composites [37] and ceramic matrix composites [38]. This jump of thermal conductivity can be associated with specific heat value, which is taken into account during calculations – equation (2).

$$\lambda(T) = \alpha(T) \cdot g(T) \cdot c_p(T) \quad (2)$$

where:

$\lambda(T)$  – thermal conductivity (W/(m·K))

$\alpha(T)$  – thermal diffusivity ( $\text{mm}^2/\text{s}$ )

$g(T)$  – density ( $\text{g}/\text{cm}^3$ )

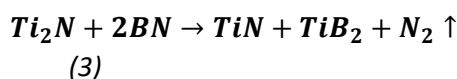
$c_l(T)$  – specific heat capacity ( $\text{J}/(\text{g}\cdot\text{K})$ )

#### 4. Discussion

The cBN-VM and cBN-CM powders used for production of sinters were described by the manufacturers as Ti-coated cBN phases, but analysis of their microstructure and phase composition showed that the main components of the coatings are titanium nitrides, i.e. TiN and  $\text{Ti}_2\text{N}$  for cBN-VM and cBN-CM powders, respectively (Fig. 1, Table 1). Titanium nitrides

with different stoichiometry was probably in-situ formed during the coating processes due to the high reactivity of metallic titanium with boron nitride [39]. The main difference between the cBN powders was the particle size, which was around 1  $\mu\text{m}$  for the cBN-0 powder, 10  $\mu\text{m}$  for the cBN-VM powder and close to 20-30  $\mu\text{m}$  for the cBN-CM powder (Fig. 1). After HPHT sintering, the cBN particle size in both powders remain at the same level. Furthermore, the powders differed also in the thickness of the coating applied on them. The one applied to cBN-CM particles was significantly thicker than that applied to cBN-VM particles. From the SEM images, it can be seen (Fig. 3 and Figs. 6 and 7), that a microstructure consisting of cBN grains surrounded by a continuous network of bonding material was formed in both cBN-VM and cBN-CM polycrystals. The cBN particles, when subjected to simultaneous high pressure and temperature, regrouped, aligned with each other and were well fused by the bonding phase eliminating practically all of the major porosity (Fig. 3 and Figs. 6 and 7). The microstructure of the cBN-0 sinter was different, as in this case the titanium based coating was unevenly applied to the cBN particles, which was most likely caused by powders agglomerating during the coating process. Such clustering promotes uneven coating distribution, which is especially apparent in case of thin encapsulation layers applied to the powders. Therefore, some of the cBN boundaries remain free of any titanium compounds after HPHT sintering (Fig. 4 and Fig. 5).

The X-ray measurements showed, that in case of the cBN-VM powder, the peaks characteristic of TiN were low in intensity and broad, indicating that the binding layer of the cBN particles consisted of ultra-fine or even poorly crystalline material (Fig. 2). As a result of HPHT sintering, the TiN-derived reflexes become narrow and intense, as well as reflexes associated with the newly formed TiB<sub>2</sub> phase appeared. In addition, a small amount of TiO<sub>2</sub> was identified in the sintered polycrystal. The crystallization of TiN and TiB<sub>2</sub> is a typical phenomenon occurring in the BN-Ti system at high temperature [13,39–41]. TiO<sub>2</sub>, on the other hand, is probably formed by the reaction of residual oxygen adsorbed on the coated cBN particles with the titanium contained in the coating. The phase evolution occurring during sintering in the cBN-CM polycrystal is very similar. In the starting powder, low-intensity and broadened reflexes originating from titanium nitride with Ti<sub>2</sub>N stoichiometry and a small amount of metallic titanium are identified. During sintering, the reaction between the titanium and boron nitride phases produces titanium nitride with a higher filling of octahedral gaps, with TiN<sub>1-x</sub> stoichiometry. It is noteworthy that during short and intensive sintering, crystallization of titanium boride with an AlB<sub>2</sub>-type layered structure also occurs. According to the literature [41], the reactions that produce TiN and TiB<sub>2</sub> can proceed as follows (Eq. 3-6):



The microstructure observations performed using the TEM method are in agreement with the XRD phase composition analysis and the SEM microstructure micro-analysis. Comparison of TEM microstructure images of cBN-VM and cBN-CM polycrystals (Fig. 8 and Fig. 9) confirm the differences in thickness of the bonding layers observed in the scanning SEM microscope. The bonding layers in the cBN-VM sinter are no thicker than 500 nm and consist of nanometric, differently oriented TiN and TiB<sub>2</sub> grains. The bonding layers in the cBN-CM polycrystal are noticeably thicker (approximately 1000-1500 nm) and are composed of sub-layers, TiO<sub>2</sub>, TiN, TiB<sub>2</sub> and TiN, presented in order from the border with the cBN particles to the center of the layer (Fig. 10). The grains of which the layers are made up are also in this case nanometric. In the latter case it indicates, that there were still some metallic titanium capable to react with the cBN crystallites during HPHT sintering process.

Significant differences in electrical conductivity of measured samples, c.a. 7 orders of magnitude, can be observed (Figs. 11-13). The highest conductivity can be observed for cBN-CM sample (Fig. 13), while the lowest conductivity was found in the case of cBN-0 sample (Fig. 13). Such behaviour can be correlated with the phase composition of the samples. In the case of the cBN-0 sample with the lowest electrical conductivity the amount of highly conductive phases TiN and TiB<sub>2</sub> (with specific electrical resistance of  $20\text{-}30\cdot 10^{-6}\ \Omega\cdot\text{cm}$  and  $9\text{-}15\cdot 10^{-6}\ \Omega\cdot\text{cm}$ , respectively [28,36,42–45]) is rather negligible. In this case the total conductivity is controlled with the predominant cBN phase (specific electrical resistance of  $10^9 - 10^{17}\ \Omega\cdot\text{cm}$  [36,42,43]). In the case of cBN-VM and cBN-CM samples observed much higher electrical conductivities can be explained by the presence of highly conductive TiN and TiB<sub>2</sub> phases and the formation of conductive percolation paths in the materials. It is also worth to notice that the conduction mechanism of cBN-VM and cBN-0 samples depends on the temperature range and differs strongly. At lower temperatures (below 500-600 °C) electrical conductivity of both samples can be described as thermally activated semiconductor behaviour. At higher temperatures, cBN-VM sample exhibit typical metallic behaviour, while cBN-0 sample changes the temperature dependence slope, but the semiconductor behaviour is still observed. The explanation of such behaviour in composite materials with complex phase composition is a difficult task and can be done taking into account the phase composition, microstructure, temperature dependence of the double barrier layer formation at the interfaces and the percolation mechanism of electrical conductivity.

On the contrary, the cBN-CM sample exhibit typical metallic behaviour in the whole temperature range, which can be explained by the presence of highly conductive TiN and TiB<sub>2</sub> as continuous phases which controls the overall electrical properties of the material (Fig. 3, Fig. 7 and Fig. 9).

The thermal conductivity of ceramic polycrystals depends on many structural and microstructural factors [46]. Among the microstructural factors affecting the value of thermal conductivity, it is worth mentioning: grain size, defects such as pores and intergrain boundaries or the presence of other phases [46]. In the investigated cBN polycrystals bonded with titanium phases, the influence of all the above-mentioned factors on the value of the thermal conductivity coefficient can be found. Figure 17 illustrates the variation of the thermal

conductivity coefficient for the three studied cBN polycrystals. The highest thermal conductivity values are recorded for the cBN-0 polycrystal, i.e. the polycrystal with the lowest content of binding titanium phases. The cBN-VM polycrystal shows intermediate thermal conductivity values and the cBN-CM sinter has the lowest values. In all cases, the thermal conductivity values decrease with increasing temperature. Similar heat conduction coefficient variations for cBN polycrystals in the temperature range 20-300 °C can be found in the work [35].

In the paper [35], it was found that the thermal conductivity depends on the cBN grain size. A large cBN grain size has a negative effect on thermal transport due to the 'weak bonding' of the grains. Furthermore, the authors of the paper [35] showed that increasing hBN content in cBN has a significant effect on thermal properties. The heat conductivity of cBN pure material was also explained by Corrigan in 1979 [47]. In contrast, work [47] found that in cubic boron nitride thermal energy is transported by vibrations in the cBN lattice and that only phonon-phonon interactions play a key role in heat transport. In the case of very fine cBN crystallites, it has been shown that the appearance of grain boundaries causes phonon scattering. It was further found that an increase in crystallite size translates into higher thermal conductivity especially at elevated temperatures. It can therefore be surmised that, in the case of cBN-0 sinter with a fine-grained microstructure, multiple intergranular boundaries have the greatest influence on phonon scattering (Fig. 15).

The decrease of cBN-VM and cBN-CM thermal conductivity above 100 °C (Fig. 15) can be attributed within interboundary phases, which contain Ti, C, N, B. For such phases, in accordance with Slack equations [46], mean free phonon path goes in nanometric scale. Hence at room temperature the mean free path is much smaller than thickness of the introduced phases between cBN grains and also their grain size [48]. The anharmonic vibration, when there are different atoms in the structure, increases with temperature what causes scattering of phonon wave. The bonding phase between cBN grains states a strong resistance for heat transport due to phonon scattering when its thickness is greater than or equal to the free path of the phonon wave  $>200$  nm, 370 [49]. The microstructure of the crystalline boundary (Figs. 9 and 10), built from various phases, is very fine with lots of irregular grains below 250 nm. The grains are finer when they are close to the cBN grain surface. Fine grains above mean free path length of phonon will have an influence on a decrease of thermal conductivity properties. The higher temperature, the shorter phonon free path and the smaller defects will play significant role at thermal conductivity. Also, scientist showed [49] that unklapp scattering take 27% of total scattering. They showed also that phonon mean free path is around 370 nm at RT and at normal pressure.

Debye's temperature plays a major role in heat conduction. At temperatures close to 0 K, the thermal conductivity is equal to the specific heat of the material. Well above the Debye's temperature, the number of phonons increases proportionally with temperature, in which case phonon-phonon interactions become responsible for heat conduction. For cBN materials Debye temperature is very high and in case of major cBN phase and it is about 1257 °C [50] (1530 K). In contrast, the Debye temperature for phases placed between cBN grains has

following values: 1175 K for  $\text{TiB}_2$  (2.2 – 3.8 wt.%), 756K for  $\text{TiN}$  (6.0 – 8.0 wt.%) and 943K for  $\text{TiO}_2$  (2.2 – 3.8 wt.%). Therefore, looking at  $\Theta$ D and quantity of titanium based phase, the phonon-phonon interaction will have significant role in case of titanium nitride [45,51,52].

In the case of titanium nitride, the fine grain size, orientation and grain boundaries affect the thermal properties, primarily causing a decrease in thermal conductivity [53,54] (Figs. 8-10). In the case of a fine microstructure, phonon scattering increases at grain boundaries, which can occur in cBN-VM and cBN-CM sinters. Phonon scattering can also be increased by lattice distortion, which is possible in the cBN composites studied, and is due to the high-pressure-high-temperature sintering technique used. Also, the presence of interstitial nitrogen atoms can generate local stresses causing phonon dispersion in the regular  $\text{TiN}$  lattice [54]. In summary, thermal stresses and a reduction in grain size can reduce the average free path of phonons and, therefore, the investigated cBN polycrystals do not show very high thermal conductivity values (Fig. 15).

Between the cBN grains there is also  $\text{TiB}_2$ , which exhibits both electron and phonon thermal conductivity. Williams' explanation [55] points out that at lower temperatures phonons are scattered by electrons, and it is the electron component of thermal conductivity that plays a major role. Similar conclusions can be found in the work of [28] in which it was found that the thermal diffusivity of titanium diboride decreases rapidly up to 600 °C, and that at higher temperatures the change in diffusivity values slows down.

Titanium dioxide  $\text{TiO}_2$  is present in cBN polycrystals in trace amounts and is found as a very thin layer on the surface of cBN grains (Figs 8-10). Titanium (IV) oxide can affect the thermal conductivity of samples in the elevated temperature range, where high-frequency phonon wave scattering must be considered [13].

In summary, the effect of all the crystalline phases present in the cBN particle-binding layers is similar, these phases scatter phonons so that the thermal conductivity of the polycrystals decreases as a function of temperature (Fig. 15).

From the point of view of cutting tools, the conversion of cBN to hBN during material machining at elevated temperatures is due to the lower thermal conductivity of cBN-based materials [56]. The hexagonal BN becomes a protective layer causing reduced tool wear. Thus, the poorer thermal conductivity at elevated temperatures can support the performance of the cutting tool.

The combination of very high mechanical properties, as well as favourable thermo-electrical characteristics, making the investigated materials promising candidates for applications in advanced cutting tools. This is especially relevant in ongoing research on smart tools capable of self-diagnosing wear status based on changes in electrical properties during cutting [57,58]. In the next stages of work, it is planned to use the obtained PcBN materials to produce cutting inserts, which will be tested during turning of difficult-to-cut workpieces.

## 5. Summary

Two commercially available Ti-coated cBN powders, cBN-VM and cBN-CM, were successfully used to create HPHT sintered PcBN composite materials without any additional

bonding phase. This approach resulted in a homogeneous microstructure without the need for homogenization, which is typically required for composites made from powder mixtures. Additionally, an in-house Ti-coated cBN powder (cBN-0) was produced using magnetron sputtering. Although the coating was inhomogeneous, with some particles lacking titanium, the sintered material was pore-free and exhibited very high Young's modulus and hardness. All the sintered composites were dense, with Young's modulus ranging from 620 to 850 GPa and hardness between 30 and 67 GPa, depending on the powder used.

XRD analysis of the starting powders revealed that the coatings contained not only Ti, as claimed by the manufacturers, but also titanium compounds, primarily TiN in cBN-VM and Ti<sub>2</sub>N and TiB in cBN-CM. This suggests that the coatings were formed during the ACT processes, where titanium reacted with BN at the powder coating stage. During the HPHT process, further reactions occurred between titanium phases and cBN. Consequently, the sintered compacts, regardless of the starting powder used, finally comprised cBN, TiN, TiB<sub>2</sub>, and a small amount of TiO<sub>2</sub>.

The measured samples exhibit substantial differences in electrical conductivity, spanning approximately seven orders of magnitude, with cBN-CM exhibiting the highest and cBN-0 the lowest values. The low conductivity of the cBN-0 material is primarily due to its minimal presence of highly conductive phases, TiN and TiB<sub>2</sub>, which have specific electrical resistances significantly lower than that of the predominant cBN phase. In contrast, the higher conductivities observed in cBN-VM and cBN-CM samples can be attributed to the abundance of these conductive phases and their ability to form effective percolation paths. The conduction mechanisms for cBN-VM and cBN-0 samples vary with temperature. At lower temperatures, both exhibits thermally activated semiconductor behaviour; however, at elevated temperatures, cBN-VM transitions to metallic behaviour while cBN-0 maintains semiconductor characteristics with altered temperature dependence. Conversely, the cBN-CM sample consistently displays metallic behaviour across all temperature ranges due to its continuous conductive phases.

The investigated composites demonstrate relatively high thermal conductivities; however, these values are significantly lower than those of typical pure dense PcBN. This reduction is primarily attributed to the presence of TiN and TiB<sub>2</sub> phases, which have lower conductivities than cBN, along with phonon scattering caused by microstructural defects and grain boundaries. The observed decrease in thermal conductivity with increasing temperature can be explained by enhanced phonon scattering associated with thermal lattice vibrations.

The combination of favourable mechanical properties and thermo-electrical characteristics, making the investigated materials promising candidates for applications in smart cutting tools capable of self-diagnosing wear status.

## **Acknowledgements**

Sintering of materials and their basic assessment were carried out within the DURACER project, entitled "Durable ceramic composites with super-hard particles for wear-resistant cutting tools", co-founded by the Polish National Centre for Research and Development within

the framework of the M-ERA.NET programme (Agreement No. M-ERA.NET2/2017/1/2018). The SEM investigations were supported by the program Excellence Initiative—Research University for the AGH University of Krakow, Grant ID 1449 (PI: M. Ziabka).

## References:

- [1] S. Malkin, Current Trends in CBN Grinding Technology, *CIRP Ann.* 34 (1985) 557–563. [https://doi.org/10.1016/S0007-8506\(07\)60188-7](https://doi.org/10.1016/S0007-8506(07)60188-7).
- [2] S.N. Monteiro, A.L.D. Skury, M.G. De Azevedo, G.S. Bobrovnitchii, Cubic boron nitride competing with diamond as a superhard engineering material - An overview, *J. Mater. Res. Technol.* 2 (2013) 68–74. <https://doi.org/10.1016/j.jmrt.2013.03.004>.
- [3] Z. Rao, W. Ding, Y. Zhu, J. Xu, Numerical simulation analysis and experimental validation on wear/fracture mechanisms of polycrystalline cubic boron nitride superabrasives in high-speed grinding, *Ceram. Int.* 45 (2019) 3377–3389. <https://doi.org/10.1016/j.ceramint.2018.10.252>.
- [4] J. Dai, Y. Li, D. Xiang, The mechanism investigation of ultrasonic roller dressing vitrified bonded CBN grinding wheel, *Ceram. Int.* 48 (2022) 24421–24430. <https://doi.org/10.1016/j.ceramint.2022.05.049>.
- [5] B. Guo, Q. Meng, G. Wu, Q. Zhao, S. Li, Parallel axis precision grinding of micro-tooth internal thread with the coarse-grains CBN wheels, *J. Manuf. Process.* 74 (2022) 474–485. <https://doi.org/10.1016/j.jmapro.2021.12.042>.
- [6] Element Six, Innovative synthetic diamond and cBN grit solutions, *Elem. 6 Broch.* (2021) 1–12. <https://e6-prd-cdn-01.azureedge.net/mediacontainer/medialibraries/element6/documents/brochures/grits-precision-grinding-brochure.pdf?ext=.pdf> (accessed August 2, 2024).
- [7] Element Six, Micron +™ finishing, *Elem. 6 Broch.* (2021) 1–8. <https://e6-prd-cdn-01.azureedge.net/mediacontainer/medialibraries/element6/documents/brochures/micron-finishing-brochure.pdf?ext=.pdf> (accessed August 2, 2024).
- [8] J. Angseryd, M. Elfving, E. Olsson, H.-O. Andrén, Detailed microstructure of a cBN based cutting tool material, *Int. J. Refract. Met. Hard Mater.* 27 (2009) 249–255. <https://doi.org/10.1016/j.ijrmhm.2008.09.008>.
- [9] S.N. Monteiro, A.L.D. Skury, M.G. de Azevedo, G.S. Bobrovnitchii, Cubic boron nitride competing with diamond as a superhard engineering material – an overview, *J. Mater. Res. Technol.* 2 (2013) 68–74. <https://doi.org/10.1016/j.jmrt.2013.03.004>.
- [10] A. Ueda, N. Watanobe, Y. Ishida, M. Abe, T. Higashi, Sumiboron Binderless Tools for Finishing Difficult-to-Cut Materials, *Tech. Rev.* 92 (2021) 20–25.
- [11] Y. Ichida, H. Ohfuchi, T. Irifune, T. Kunimoto, Y. Kojima, T. Shinmei, Synthesis of coarse-grain-dispersed nano-polycrystalline cubic boron nitride by direct transformation under ultrahigh pressure, *Diam. Relat. Mater.* 77 (2017) 25–34. <https://doi.org/10.1016/j.diamond.2017.04.020>.
- [12] E. Piskorska, K. Ławniczak-Jabłońska, E. Benko, I.N. Demchenko, P. Klimczyk, E. Welter, R.C.C. Perera, P. Nachimuthu, Chemical activations of the binding phase formation in cBN composites, *Synchrotron Radiat. Nat. Sci. Bull. Polish Synchrotron Radiat. Soc.* 1 (2002) 42.
- [13] Y. Liu, W. Zhang, Y. Peng, G. Fan, B. Liu, Effects of TiAl Alloy as a Binder on Cubic Boron Nitride Composites, *Materials (Basel)*. 14 (2021) 6335. <https://doi.org/10.3390/ma14216335>.
- [14] V. Turkevich, T. Taniguchi, A. Andreev, P. Itsenko, Kinetics and mechanism of cubic boron nitride formation in the AlN-BN system at 6 GPa, *Diam. Relat. Mater.* 13 (2004) 64–68. <https://doi.org/10.1016/j.diamond.2003.08.020>.
- [15] K. Katuku, A. Koursaris, I. Sigalas, High-temperature stability of polycrystalline cubic boron nitride cutting tool materials in air, *Corros. Sci.* 64 (2012) 55–63. <https://doi.org/10.1016/j.corsci.2012.07.002>.

- [16] L. Tu, L. Lin, C. Liu, T. Zheng, Y. Deng, L. Han, Q. An, W. Ming, M. Chen, Tool wear characteristics analysis of cBN cutting tools in high-speed turning of Inconel 718, *Ceram. Int.* 49 (2023) 635–658. <https://doi.org/https://doi.org/10.1016/j.ceramint.2022.09.034>.
- [17] Coated Borazon™ BMP™ Powders, (2024). <https://www.hyperionmt.com/en/products/Abrasives/micron-cbn/coated-borazon-bmp/>.
- [18] W. Mohamed Daoush, T. Saad Alkhurajji, A.D. Alshammri, Fabrication of Polycrystalline Cubic Boron Nitride/Metal Composite Particles by Surface Metallization Followed by Electroless Deposition Technique, *Materials (Basel)*. 14 (2021) 7906. <https://doi.org/10.3390/ma14247906>.
- [19] D. Chen, Z. Liu, B. Fan, J. Li, W. Cao, H. Wang, H. Lu, H. Xu, R. Zhang, Synthesis and Characterization of TiN-coated Cubic Boron Nitride Powders, *Int. J. Appl. Ceram. Technol.* 11 (2014) 946–953. <https://doi.org/10.1111/ijac.12080>.
- [20] P. Klimczyk, E. Benko, K. Lawniczak-Jablonska, E. Piskorska, M. Heinonen, A. Ormaniec, W. Gorczynska-Zawislana, V.S. Urbanovich, Cubic boron nitride - Ti/TiN composites: hardness and phase equilibrium as function of temperature, *J. Alloys Compd.* 382 (2004) 195–205. <https://doi.org/10.1016/j.jallcom.2004.04.140>.
- [21] Y. Liu, W. Zhang, Y. Peng, G. Fan, B. Liu, Effects of TiAl Alloy as a Binder on Cubic Boron Nitride Composites, *Materials (Basel)*. 14 (2021) 6335. <https://doi.org/10.3390/ma14216335>.
- [22] J. Morgiel, P. Klimczyk, R. Lach, A. Gubernat, Microstructure and phase composition of Ti-coated cBN powders intended for active coating technology (ACT) processes, *Appl. Surf. Sci.* 680 (2025) 161378. <https://doi.org/10.1016/j.apsusc.2024.161378>.
- [23] D. Shaw, J. Kulczyk-Malecka, P.J. Kelly, A.M. Doyle, Methane oxidation over supported Pd catalysts prepared by magnetron sputtering, *Surf. Coatings Technol.* 414 (2021) 127123. <https://doi.org/https://doi.org/10.1016/j.surfcoat.2021.127123>.
- [24] A.I. Prikhna, High Pressure Apparatuses in Production of Synthetic Diamonds (Review), *J. Superhard Mater.* 30 (2008) 1–15. <https://doi.org/DOI: 10.3103/S1063457608010012>.
- [25] L.G. Khvostantsev, V.N. Slesarev, V. V. Brazhkin, Toroid type high-pressure device: history and prospects, *High Press. Res.* 24 (2004) 371–383. <https://doi.org/10.1080/08957950412331298761>.
- [26] L. Vel, G. Demazeau, J. Etourneau, Cubic boron nitride: synthesis, physicochemical properties and applications, *Mater. Sci. Eng. B.* 10 (1991) 149–164. [https://doi.org/10.1016/0921-5107\(91\)90121-B](https://doi.org/10.1016/0921-5107(91)90121-B).
- [27] M.P. D'Evelyn, K. Zgonc, Elastic properties of polycrystalline cubic boron nitride and diamond by dynamic resonance measurements, *Diam. Relat. Mater.* 6 (1997) 812–816. [https://doi.org/10.1016/s0925-9635\(96\)00631-0](https://doi.org/10.1016/s0925-9635(96)00631-0).
- [28] R.G. Munro, Material Properties of Titanium Diboride, *J. Res. Natl. Inst. Stand. Technol.* 105 (2000) 709–720. <https://doi.org/10.6028/jres.105.057>.
- [29] J. Russias, S. Cardinal, C. Esnouf, G. Fantozzi, K. Bienvenu, Hot pressed titanium nitride obtained from SHS starting powders: Influence of a pre-sintering heat-treatment of the starting powders on the densification process, *J. Eur. Ceram. Soc.* 27 (2007) 327–335. <https://doi.org/10.1016/j.jeurceramsoc.2006.02.032>.
- [30] L. Vel, G. Demazeau, J. Etourneau, Cubic boron nitride: synthesis, physicochemical properties and applications, *Mater. Sci. Eng. B.* 10 (1991) 149–164. [https://doi.org/10.1016/0921-5107\(91\)90121-B](https://doi.org/10.1016/0921-5107(91)90121-B).
- [31] H. Sumiya, Y. Ishida, K. Arimoto, K. Harano, Real indentation hardness of nano-polycrystalline cBN synthesized by direct conversion sintering under HPHT, *Diam. Relat. Mater.* 48 (2014) 47–51. <https://doi.org/10.1016/j.diamond.2014.06.009>.
- [32] G. Berg, C. Friedrich, E. Broszeit, C. Berger, Data Collection of Properties of Hard Material, in: *Handb. Ceram. Hard Mater.*, Wiley, 2000: pp. 965–995. <https://doi.org/10.1002/9783527618217.ch24>.
- [33] M.G. Loshak, L.I. Aleksandrova, The effect of the indentation load on the results of measuring hardness of superhard materials, *J. Superhard Mater.* 34 (2012) 305–307.

- <https://doi.org/10.3103/S1063457612050036>.
- [34] B.G.A. Brito, L. Cândido, Thermodynamic properties of cubic boron-nitride crystal by path integral Monte Carlo simulations, *Chem. Phys. Lett.* 751 (2020) 137513. <https://doi.org/https://doi.org/10.1016/j.cplett.2020.137513>.
- [35] C. Leng, X. Hu, H. Xie, C. Shen, Thermal properties of polycrystalline cubic boron nitride sintered under high pressure condition, *Sci. Sinter.* 50 (2018) 401–408. <https://doi.org/10.2298/SOS1804401L>.
- [36] H.O. Pierson, *Handbook of Refractory Carbides and Nitrides Properties, Characteristics, Processing and Applications*, Noyes Publications, Westwood, New Jersey, 1996.
- [37] P.F. Wang, Z.H. Li, Y.M. Zhu, Fabrication of high thermal conductive Al–cBN ceramic sinters by high temperature high pressure method, *Solid State Sci.* 13 (2011) 1041–1046. <https://doi.org/10.1016/j.solidstatesciences.2011.01.023>.
- [38] V. Bushlya, I. Petrusha, O. Gutnichenko, O. Osipov, R. M'Saoubi, V. Turkevich, J.-E. Ståhl, Sintering of binderless cubic boron nitride and its modification by  $\beta$ -Si<sub>3</sub>N<sub>4</sub> additive for hard machining applications, *Int. J. Refract. Met. Hard Mater.* 86 (2020) 105100. <https://doi.org/10.1016/j.ijrmhm.2019.105100>.
- [39] P. Klimczyk, E. Benko, K. Lawniczak-Jablonska, E. Piskorska, M. Heinonen, A. Ormaniec, W. Gorczynska–Zawislan, V.S. Urbanovich, Cubic boron nitride - Ti/TiN composites: hardness and phase equilibrium as function of temperature, *J. Alloys Compd.* 382 (2004) 195–205. <https://doi.org/10.1016/j.jallcom.2004.04.140>.
- [40] E. Benko, P. Klimczyk, J. Morgiel, A. Włochowicz, T.L. Barr, Electron microscopy investigations of the cBN–Ti compound composites, *Mater. Chem. Phys.* 81 (2003) 336–340. [https://doi.org/10.1016/S0254-0584\(03\)00016-6](https://doi.org/10.1016/S0254-0584(03)00016-6).
- [41] R. Mineiro, C.M. Fernandes, E.L. Silva, M.R. Soares, D. Figueiredo, B. Ferrari, A.J. Sanchez-Herencia, A.M.R. Senos, Reaction behavior during Spark Plasma Sintering of cBN–TiCN–Ni powders, *J. Eur. Ceram. Soc.* 43 (2023) 6783–6792. <https://doi.org/10.1016/j.jeurceramsoc.2023.06.074>.
- [42] A.W. Weimer, ed., *Carbide, Nitride and Boride Materials Synthesis and Processing*, Springer Netherlands, Dordrecht, 1997. <https://doi.org/10.1007/978-94-009-0071-4>.
- [43] R. Telle, L.S. Sigl, K. Takagi, Boride-Based Hard Materials, in: R. Riedel (Ed.), *Handb. Ceram. Hard Mater.*, WILEY-VCH, Weinheim, 2000: pp. 802–945.
- [44] A. Suri, N. Krishnamurthy, C. Subramanian, Issues in the synthesis and fabrication of refractory carbides, borides, silicides and their mixtures, in: O. Tatsuki, M. Sing (Eds.), *Advanced Process. Munufacturing Technol. for Struct. Multifunct. Mater. II*, A John Wiley & Sons, Inc., Hoboken, New Jersey, 2010: pp. 69–79.
- [45] F.W. Vahldiek, Electrical resistivity, elastic modulus, and debye temperature of titanium diboride, *J. Less Common Met.* 12 (1967) 202–209. [https://doi.org/10.1016/0022-5088\(67\)90115-4](https://doi.org/10.1016/0022-5088(67)90115-4).
- [46] G.A. Slack, The Thermal Conductivity of Nonmetallic Crystals, *Solid State Phys.* 34 (1979) 1–71. [https://doi.org/10.1016/S0081-1947\(08\)60359-8](https://doi.org/10.1016/S0081-1947(08)60359-8).
- [47] F.R. Corrigan, Thermal Conductivity of Polycrystalline Cubic Boron Nitride Compacts, in: *High-Pressure Sci. Technol.*, Springer US, Boston, MA, 1979: pp. 994–999. [https://doi.org/10.1007/978-1-4684-7470-1\\_133](https://doi.org/10.1007/978-1-4684-7470-1_133).
- [48] G.A. Slack, R.A. Tanzilli, R.O. Pohl, J.W. Vandersande, The intrinsic thermal conductivity of AlN, *J. Phys. Chem. Solids.* 48 (1987) 641–647. [https://doi.org/10.1016/0022-3697\(87\)90153-3](https://doi.org/10.1016/0022-3697(87)90153-3).
- [49] S. Mukhopadhyay, D.A. Stewart, Polar effects on the thermal conductivity of cubic boron nitride under pressure, *Phys. Rev. Lett.* 113 (2014) 1–5. <https://doi.org/10.1103/PhysRevLett.113.025901>.
- [50] B.P. Pandey, V. Kumar, Heat Capacity of BN and GaN binary semiconductor under high Pressure-Temperature (PT) from First-principles, *IOSR J. Appl. Phys.* 4 (2013) 42–48.
- [51] A. Kozma, Thermodynamic, thermal and elastic properties of titanium nitride tin: comparison of various data and determination of the most reliable values, *Technol. Transf. Fundam. Princ.*

- Innov. Tech. Solut. 4 (2020) 14–17. <https://doi.org/10.21303/2585-6847.2020.001475>.
- [52] Titanium dioxide, IARC Monogr. Eval. Carcinog. Risks to Humans. 93 (2010) 193–214. <https://doi.org/10.4011/shikizai.84.104>.
- [53] M.K. Samani, X.Z. Ding, N. Khosravian, B. Amin-Ahmadi, Y. Yi, G. Chen, E.C. Neyts, A. Bogaerts, B.K. Tay, Thermal conductivity of titanium nitride/titanium aluminum nitride multilayer coatings deposited by lateral rotating cathode arc, *Thin Solid Films*. 578 (2015) 133–138. <https://doi.org/10.1016/j.tsf.2015.02.032>.
- [54] A. Albert Irudayaraj, R. Srinivasan, P. Kuppusami, E. Mohandas, S. Kalainathan, K. Ramachandran, Photoacoustic measurement of thermal properties of TiN thin films, *J. Mater. Sci.* 43 (2008) 1114–1120. <https://doi.org/10.1007/s10853-007-2248-8>.
- [55] R.K. Williams, R.S. Graves, F.J. Weaver, Transport properties of high purity, polycrystalline titanium diboride, *J. Appl. Phys.* 59 (1986) 1552–1556. <https://doi.org/10.1063/1.336463>.
- [56] X. Ding, W.Y.H. Liew, B.K.A. Ngoi, J.G.K. Gan, S.H. Yeo, Wear of CBN tools in ultra-precision machining of STAVAX, *Tribol. Lett.* 12 (2002) 3–12.
- [57] R. Daicu, G. Oancea, Methodology for Measuring the Cutting Inserts Wear, *Symmetry (Basel)*. 14 (2022) 469. <https://doi.org/10.3390/sym14030469>.
- [58] R. Daicu, G. Oancea, Electrical Current at Metal Cutting Process: A Literature Review, *Appl. Mech. Mater.* 808 (2015) 40–47. <https://doi.org/10.4028/www.scientific.net/AMM.808.40>.